Implementation of grain mapping by diffraction contrast tomography on a conventional laboratory tomography setup with various detectors

Haixing Fang, Wolfgang Ludwig, Pierre Lhuissier

▶ **To cite this version:**

Haixing Fang, Wolfgang Ludwig, Pierre Lhuissier. Implementation of grain mapping by diffraction contrast tomography on a conventional laboratory tomography setup with various detectors. JOURNAL OF APPLIED CRYSTALLOGRAPHY, 2023, 56, pp.810-824. 10.1107/S1600576723003874 . hal-04305375

HAL Id: hal-04305375
https://hal.science/hal-04305375

Submitted on 24 Nov 2023

HAL is a multi-disciplinary open access archive for the deposit and dissemination of scientific research documents, whether they are published or not. The documents may come from teaching and research institutions in France or abroad, or from public or private research centers.

L'archive ouverte pluridisciplinaire **HAL**, est destinée au dépôt et à la diffusion de documents scientifiques de niveau recherche, publiés ou non, émanant des établissements d'enseignement et de recherche français ou étrangers, des laboratoires publics ou privés.

Implementation of grain mapping by diffraction contrast tomography on conventional laboratory tomography setup with variable detectors

Haixing Fang[a,b,c *], Wolfgang Ludwig[b,c], and Pierre Lhuissier[a]

[a]*Université Grenoble Alpes, Grenoble INP, CNRS SIMaP, 1130 Rue de la Piscine, 38402 Saint Martin d'Hères, France.*

[b]*European Synchrotron Radiation Facility, 71 Avenue des Martyrs, 38000 Grenoble, France.*

[c]*Université de Lyon, INSA Lyon, CNRS MATEIS, 69621 Villeurbanne, France.*

[*]Corresponding author: Haixing Fang, haixing.fang@grenoble-inp.fr; haixingfang868@gmail.com

Abstract

Lab-based diffraction contrast tomography (LabDCT) is a novel technique to resolve grain orientations and shapes in 3D at the micron scale using laboratory X-ray sources, lifting out the constraint of limited access to synchrotron facilities. To foster the development of this technique, detailed implementation of LabDCT is illustrated on a conventional lab-based X-ray tomography setup and it is shown that such implementation is possible with the two most common types of detectors – CCD and flat panel. As a benchmark, LabDCT projections were acquired on an AlCu alloy sample using the two types of detectors at different exposure times. Grain maps were subsequently reconstructed using the open-sourced grain reconstruction method as reported in our previous work. To characterize the detection limit and the spatial resolution for the current implementation, the reconstructed LabDCT grain maps were compared with the one obtained from a synchrotron measurement, which is considered as ground truth. Results show that the final grain maps from measurements of the CCD and flat panel detector are similar and show comparable quality, whilst the CCD gives a much better contrast-to-noise ratio than the flat panel. The analysis of grains maps reconstructed from measurements with different exposure time suggests that a grain map of comparable quality could have been obtained in less than one hour total acquisition time without a significant loss of grain reconstruction quality and indicates a clear potential for time-lapse LabDCT experiments. The current implementation is suggested to promote the generic use of LabDCT technique for grain mapping on conventional tomography setups.

Keywords: Diffraction contrast tomography; Grain reconstruction; CCD detector; Flat panel; Synchrotron X-ray diffraction.

1. Introduction

Grain mapping techniques have seen a rapid development in the last 25 years to resolve 3D grain orientations and shapes in bulk materials at micron and nanometer scales with a particular interest of using X-rays (Poulsen, 2020). Such techniques have been well established at synchrotron facilities and led to numerous discoveries and new understandings in materials science (*e.g.* Offerman *et al*., 2002; Schmidt *et al.*, 2004; King *et al*., 2008; Simons *et al.*, 2018; Bhattacharya *et al*., 2021). Typical examples include near-field and far-field imaging techniques such as three-dimensional X-ray diffraction microscopy (3DXRD, Poulsen, 2004; Suter *et al.*, 2006; Bernier *et al*., 2011) and diffraction contrast tomography (DCT, Ludwig *et al*., 2008; Ludwig *et al*., 2009) with a spatial resolution down to 1 μm, and raster scanning techniques such as differential aperture X-ray microscopy (DAXM, Larson *et al*., 2002) and scanning 3DXRD (Hayashi *et al*., 2019; Henningsson *et al*., 2020) with a spatial resolution down to ~200 nm. Another more recent technique is X-ray dark field microscopy (Simons *et al*., 2015; Poulsen *et al*., 2017; Jakobsen *et al*., 2019), which provides both very high spatial (~100 nm) and orientation resolutions (~0.005°) and is able to map individual dislocation lines. All these techniques, however, require the use of synchrotron radiation and thus place a serious limitation of access.

To lift out this limitation and broaden the use of grain mapping techniques, lab-based X-ray diffraction contrast tomography (LabDCT), adapting from the synchrotron DCT, has been developed (King *et al*., 2013; King *et al.*, 2014) and commercialized (McDonald *et al*., 2015; McDonald *et al*., 2017). These approaches share the characteristics of using a conical polychromatic beam, confined by an aperture, to illuminate a 3D sample volume and placing a 2D detector behind the sample to record a series of diffraction projections during a stepwise 360° rotation around a vertical axis, while the direct transmitted beam is blocked by a beamstop placed in front of the detector to enhance the diffraction signals. The very first approach (King *et al*., 2013) was implemented on a conventional tomography setup with a magnified geometry (sample-to-detector distance is larger than sample-to-source distance, $L_{sd} > L_{ss}$) using a flat panel detector with a pixel size of 127 μm. Grain indexing was based on Friedel pair matching and subsequent grain shape reconstruction was performed using algebraic reconstruction techniques, based on iterative forward and back projections. This approach, however, can only deal with moderate number of grains in the illuminated sample volume to avoid overlap of diffraction spots. The commercial approach, based on a forward modeling strategy, was implemented on Zeiss Xradia setups as an additional modality, using either a Laue focusing geometry ($L_{sd} = L_{ss}$) with a high resolution CCD detector (*e.g*. Zeiss Xradia 520 Versa), or a magnified geometry with a flat panel (*e.g.* Zeiss Xradia CrystalCT) (Bachmann *et al.*, 2019; Oddershede *et al*., 2022). A commercial software GrainMapper3D developed by XnovoTech, based on forward projection (Bachmann *et al.*, 2019), offers an easy-to-use and robust method for grain reconstruction. However, this implementation is restricted to a specific instrument and requires a commercial license. This means that other types of widely available laboratory μ-CT instruments cannot have access to GrainMapper3D and cannot be used for LabDCT experiments.

To truly boost the use of grain mapping by LabDCT, robust and computationally efficient grain reconstruction methods have been developed based on forward and back calculations running on a graphical processing unit (GPU) (Fang *et al*., 2022b). A first experimental demonstration was reported in (Fang *et al*., 2022a), providing limited technical details on the implementation. To follow up, in this work we show detailed experimental implementation of this LabDCT technique on a conventional tomography instrument using two most common types of detectors - CCD and flat panel detector. An AlCu alloy sample was used as a benchmark for testing these two different instrument configurations, from which 3D grain maps were reconstructed using our previously developed method. To verify the LabDCT grain maps, we performed synchrotron DCT measurement on the same sample and used the synchrotron reconstructed grain map as ground truth for comparison. Results show that most grains were successfully mapped, whilst some small grains failed to be reconstructed because of their poorer detectability. To provide a guideline for setting up optimal acquisition time, we determined contrast-to-noise ratios as a function of grain size and exposure time for the two different detectors and compared the corresponding grain reconstruction results. Detection limit and spatial resolution are quantified for the current implementation of the LabDCT technique. The performance using different detectors is compared and discussed in detail. Ultimately, an outlook for further developing the LabDCT technique is presented.

Notably, the purpose of this study is not to provide exhaustive sample measurements nor to optimize the grain mapping performance in a general sense for different types of tomography instruments as they differ in source, detector and geometry constraints *etc*. Instead, this study shows an example implementation of grain mapping on a conventional tomography setup and present the typical performance and limits related to the experimental conditions and instrument, which may serve as a guideline for researchers who wish to implement the LabDCT technique on their own X-ray tomography instruments.

2. Materials and methods

2.1. Sample

An AlCu alloy (8 wt.% Cu) cylindrical rod with a diameter of ~3 mm and a length of ~6 mm was annealed at 580 °C for 1 h, followed by slow cooling in a furnace at an initial cooling rate of ~3.5 °C/min, with an intention to remove lattice strains. During annealing, the sample was in a solid-liquid two-phase region, where the equilibrium fraction of the solid phase was calculated to be about 83.3% using the lever rule based on the Al-Cu phase diagram. During cooling, the Cu-enriched eutectic phase solidified, giving rise to a continuous layer of (crystallites smaller than a few microns) precipitates, delineating the grain boundaries of the solid matrix phase. Thereby, grain shapes of the Al matrix phase can be resolved by absorption contrast tomography due to significant contrast between the Cu-enriched phase and the face-cubic-centered Al.

A wedge-shaped sample (width × thickness× height ≈ 600 × 450 × 1000 µm^3) was wire-cut from the heat-treated rod. Sample surfaces were subsequently polished by fine-grid SiC papers before LabDCT and synchrotron measurements.

2.2. Laboratory tomography setup

A conventional tomography setup, EASYTOM XL Nano focus tomography manufactured by RX-solutions, was used to implement LabDCT for grain mapping. This setup is compatible with two different sources (L10711 nano source and L8121-03 micro source produced by Hamamatsu Photonics; both can be operated in small, middle and large size modes) and different detectors (CCD, flat panel *etc*.), see more details in (Fang *et al*., 2022a). The micro source is located about 15 mm behind the emission window, while the nano source sits very close (~1 mm) to the window. This makes the nano source more suitable for realizing short sample-to-source distances and consequently larger geometric magnification, and thus achieve higher spatial resolutions compared to the micro source, despite that the micro source can provide a higher flux. Tests were performed to confirm this, hence the nano source was selected for the LabDCT experiments. The maximum acceleration voltage for the nano source is 100 kV. Notably, this source can be operated with identical maximum current (30.9 µA for middle size source), independent of the acceleration voltage. Spectra tests have shown that the total photon flux has a weak correlation with source voltage, whereas the X-ray spectra differ and the fraction of high energy photons increases with increasing voltage.

The tomography instrument is equipped with an air bearing sample rotation stage (Lab Motion Systems RT100) with a maximum radial error motion of 178 nm measured at 111 mm from the top surface. This value is far smaller than the effective detector pixel size and can therefore be neglected.

Geometric constraints of the instrument may imply compromises in acquisition geometry. For the instrument described in this study, the source-to-detector distance of the CCD detector is confined to the range 60 ~ 505 mm, while this range is 230 ~ 675 mm for the flat panel. The detectors can move along the beam direction as well as in the lateral direction, whereas it cannot move vertically nor it can rotate. Detector offsets and tilts with respect to the X-ray beam need to be known with high precision and are determined via a fitting procedure described in section 3.

For LabDCT measurements, pinholes of different sizes are used to define the dimensions of the illuminated sample volume and the direct beam footprint on the detector, which both also vary as a function of distances between these elements. A motorization of the pinhole along the three principal directions with a travel range allowing for complete retraction out of the beam is highly beneficial as it allows for rapid alignment and tuning of the illuminated area in the sample and detector planes, as well as easy switching between conventional imaging and diffraction mode. For the current implementation a series of cylindrical disks made of tungsten (15.9 mm outer diameter and 2 mm thickness) with different sizes of central holes (diameter 100, 200, 400, 1000 and 2000 µm) were prepared. The 400 µm disk, most appropriate for the current sample dimension, was then be positioned as close as ~0.6 mm to the source window with a set of micro-positioning stages (Attocube, Germany). Details of this

implementation can be seen in Figure 1. A CCD (Quad-RO 4320 produced by Princeton Instruments, 24 μm^2 pixel size, 2084×2084 pixels, coupled to a 150 μm thick CsI scintillator with a taper 1:1) or a flat panel (PaxScan 2520DX from Varian Medical Systems, 127 μm^2 pixel size, 1536×1920 pixels, using a 600 μm thick CsI scintillator and an amorphous silicon architecture) was used for recording absorption tomography and DCT projections.

Experimental projections were acquired using Xact acquisition software developed by RX-solutions. This software performs image distortion correction and intensity correction but not noise filtering. The maximum exposure time for the CCD detector is 60 s and is 4 s for the flat panel.

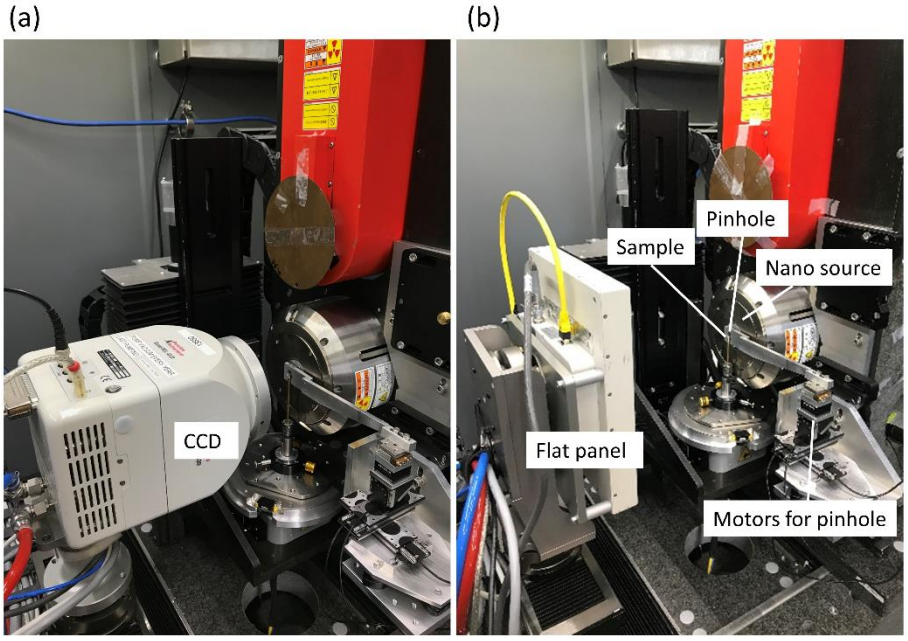

Figure 1. Photos showing the LabDCT implementation on a conventional tomography setup using (a) a CCD (effective width × height = 50.0 × 50.0 mm) and (b) a flat panel (effective width × height = 184.9 × 233.7 mm). A pinhole is placed between the sample and the nano-source, and its position is controlled by three motors. A 2 mm thick sheet of lead, covering the footprint of the direct beam, is attached onto the detector for DCT acquisition.

2.3. Data collected with the lab-based tomography instrument

Measurement on the AlCu alloy sample using the CCD was performed first. Using a conical polychromatic beam emitted from a tungsten target of the nano source (60 kV and 1.8 W, middle size), 384 absorption projections were acquired using an exposure time (t_{exp}) of 0.5 s for 4 sample turns, filling in the rotation gaps equally. This resulted in a rotation step of 0.94°. After that, a pinhole with a diameter of 400 μm was placed in between the sample and the source, and a beamstop made of Pb with a thickness of ~2 mm was pasted on a paper and placed in front of the detector to attenuate the direct transmitted beam for recording DCT projections. The DCT acquisition was performed with the same source voltage of 60 kV but with a maximum allowed input current of 120 μA, reaching a power of 7.2 W and a current

of 30.9 μA on the transmission target of the source to maximize the photon flux (note that the current on the target is smaller than the input current). Projection images were acquired at a step of 3° over a full sample rotation of 360°. At each rotation angle, 6 frames were recorded and the exposure time for each frame was 60 s, which is the maximum for the present CCD. Projection images obtained with shorter exposure times are presented in Supplementary Materials.

After the CCD measurement, we manually replaced the detector by the flat panel without changing the sample position. The experimental procedure was repeated: first with an absorption tomography scan (4 turns with 800 projections at a rotation step of 0.45° and the source of 60 kV and 1.8 W) and then a DCT scan with 60 kV and 7.2 W source power. The DCT scan was also performed with a rotation step of 3° for 360° sample rotation, but this time, for each rotation angle 90 frames were acquired and the exposure time for each frame was 4 s (maximum for this flat panel), resulting in the same accumulated exposure time as the CCD measurement, *i.e.* 360 s per angle.

The main experimental parameters are summarized in Table 1. The sample-to-source distance (L_{ss}) was chosen to be very close (~9.2 mm) for both measurements, while the sample-to-detector distance (L_{sd}) was selected based on a combination of considerations related to (i) coverage of diffraction angles, (ii) effective pixel size in the sample plane and (iii) size of the direct beam footprint (to be covered by the beamstop). Note that further reduction of the sample-to-source distance (*i.e.* increasing the opening angle of the cone beam by using a larger pinhole) would be beneficial for optimizing flux density but also increases the footprint of the direct beam and therefore reduces the effective detector region for recording the diffraction signals. Ultimately, the effective pixel size in the sample plane for the flat panel is slightly bigger than that for the CCD. The source voltage was selected by considering the balance between a proper transmission of the X-ray beam and a suitable coverage of the most probable diffraction spot energies. In the case of AlCu alloy sample studied here, diffraction spots from the first 4 {*hkl*} families mainly have photon energies in the range of 15-45 keV based on our forward simulation (Fang *et al*., 2020) under the current experimental conditions. With additional LabDCT tests, a source voltage of 60 kV was chosen. More detailed testing result for key experimental parameters, including L_{sd}, source voltage and source size, are presented in Supplementary Materials.

Table 1. Experimental parameters for the LabDCT measurements. Zoom = 1 + L_{sd} / L_{ss}, characterizes the magnification factor; Effective pixel size is calculated as detector pixel size divided by Zoom; N_{frame} is the number of frames.

Experiment	L_{ss} (mm)	L_{sd} (mm)	Zoom (-)	Pixel size (μm)	Eff. pixel size (μm)	t_{exp} per frame (s)	N_{frame} per angle (-)
CCD	9.2	55.4	7.1	24	3.4	60	6
Flat panel	9.2	224.6	25.4	127	5.0	4	90

An absorption tomographic volume with a voxel size of 2.7 μm was reconstructed from the absorption projections, using the Xact reconstruction software developed by RX-solutions. In the sample volume, three phases were identified: Al matrix, Cu-enriched eutectic phase and cavities. A sample volume mask was defined by segmenting the Al matrix phase. Since there are much less tomography projections recorded by CCD (384 projections) than the flat panel (800 projections), the reconstructed tomography volume from the CCD acquisition has a poorer quality than the flat panel. As a result, the segmented volume mask from the CCD is noisier and the Cu-enriched eutectic phase is less well resolved compared to the flat panel.

The sample volume mask, together with the DCT projection images and acquisition geometry parameters, were used as input for 3D grain reconstruction using the method reported in our previous work (Fang *et al*., 2022b). Part of the reconstructions were performed using only sub-samples of the available projection data in order to mimic shorter exposure times. Currently, running the grain reconstruction requires a MATLAB license, but the programming code could be translated to other open source programming languages (*e.g.* Python). Details about the grain reconstruction procedure will be presented in Section 3.

2.4. Synchrotron diffraction contrast tomography

Synchrotron DCT measurement was performed on beamline ID11 of European Synchrotron Radiation Facility (ESRF). The same AlCu alloy sample was illuminated by a parallel monochromatic beam with an energy of 43.64 keV. A sCMOS (Andor Marana) detector with 2048×2048 pixels was placed at a distance of 7.2 mm from the vertical rotation axis. Diffraction signals were recorded by the outer area of the detector, while the transmitted direct beam was attenuated by a beamstop and recorded by the central area of the detector. The detector was coupled to a 10 μm thickness transparent luminescent screen via a 7.5× objective lens, resulting in an effective pixel size of 1.6 μm. A series of 3600 equally spaced projections over 360° sample rotation were acquired with an exposure time of 0.15 s for each projection. 3D grain map, together with tomographic volume with a voxel size of 1.6 μm, were reconstructed using the method described in (Ludwig *et al*., 2009; Reischig *et al*., 2013).

2.5. Comparison of reconstructed grain maps from LabDCT with synchrotron DCT

Due to its far better detection limit and spatial resolution (Reischig *et al*., 2013; Renversade *et al*., 2016; Fang, Juul Jensen *et al.*, 2021; McDonald *et al*., 2021), the grain map reconstructed from the synchrotron DCT was considered as ground truth and the result is referred to as SR-DCT. To compare the orientation and spatial deviation between the LabDCT grain maps and SR-DCT, the SR-DCT dataset was registered to the grain volume of the LabDCT dataset by resampling (voxel size increased from 1.6 to 2.7 μm, being the same as one used in the LabDCT datasets), rotating and translating the SR-DCT volume, using the same method as reported in (Fang, Juul Jensen *et al*., 2021). As the grain shapes are also revealed by the grain boundary precipitation of the Cu enriched phase, tomography volumes, reconstructed by the synchrotron and laboratory measurements, respectively, were used to further verify the accuracy of the volume registration as well as to check the accuracy of the grain shape reconstruction.

To assess how well the grain indexing is, grains were paired between the LabDCT and SR-DCT datasets based on their orientations and spatial locations. All the grains are classified into three categories: 1) true positively indexed grains (*TPs*), including one-to-one indexed and one-to-multi indexed ones (a grain in the SR-DCT dataset reconstructed as multiple grains with similar orientations in the LabDCT dataset); 2) false negatively indexed grains (*FNs*), which exist in SR-DCT but not found in the LabDCT dataset; 3) false positively indexed grains (*FPs*), which are indexed in the LabDCT dataset but not in SR-DCT. To evaluate the indexing accuracy, F_1 score was calculated from precision (P) and sensitivity (S), *i.e.* F_1 score = 2 * P * S / (P + S), where $P = TP / (TP + FP)$ and $S = TP / (TP + FN)$. The F_1 score has a value between 0 and 1, with a value closer to 1 corresponding to a better indexing performance. It is worthy to note that the F_1 score is a metric to evaluate the overall indexing performance and is calculated on a grain by grain basis, as reported elsewhere (Fang, Juul Jensen *et al*., 2021; Fang, Hovad *et al*., 2021).

For the paired grains, disorientations (Δ_{OR}) were calculated by MTEX toolbox (Bachmann *et al*., 2010) to evaluate the orientation resolution. To evaluate how well the reconstruction is for the grain shape (considered as spatial resolution), the deviations in grain center-of-mass (Δ_{grain}) and grain boundary deviation (δ_{GB}) for each grain pair were computed. δ_{GB} was calculated as

$$\delta_{GB} = \frac{1}{N_{voxel,GB}} \sum \varepsilon_{GB}, \quad (1)$$

where ε_{GB} is the Euclidean distance between a grain boundary voxel in the SR-DCT dataset and the nearest voxel on the boundary of the paired grain in the LabDCT dataset; $N_{voxel,\,GB}$ is the total number of grain boundary voxels in the SR-DCT dataset. More details about the method for the comparison can be found in (Fang, Juul Jensen *et al*., 2021; Fang, Hovad *et al*., 2021).

3. Procedure of grain reconstruction for LabDCT

Let us define a right handed laboratory coordinate system with the beam direction as x, horizontal direction y and vertical (parallel to rotation axis) direction z. To reconstruct a 3D grain map, 5 inputs must be prepared: 1) spot segmented images processed from the diffraction projections; 2) volume mask determined from the segmentation of the tomography volume (see Section 2.2); 3) geometry parameters including L_{ss}, L_{sd}, source offsets in horizontal and vertical directions (denoted as S_y and S_z, respectively), detector offsets horizontally (*dety*0) and vertically (*detz*0) and tilts about x, y and z axes (φ_x, φ_y and φ_z, respectively); 4) lattice parameters of the sample; 5) reconstruction parameters. In the current work, we restrict our LabDCT grain mapping on samples with a *priori* known crystal structure and negligible lattice strains.

We choose the LabDCT measurement on the AlCu alloy sample with the CCD detector to illustrate the grain reconstruction procedure. Figure 2 shows the image processing procedure. Figure 2a shows one experimental image averaged over six CCD frames, corresponding to an exposure time of 360 s (6 frames × 60 s per frame). Then, a flat field correction using the same method as reported in

(Lindkvist *et al*., 2021) was applied and the contrast between the spot and the background is enhanced (Figure 2b). Subsequently, a rolling median background correction was performed (Figure 2c). Last, a Laplacian of Gaussian based method (Lind 2013; Bachmann *et al*., 2019; Fang, Juul Jensen *et al*., 2021) was used to segment the diffraction spots (Figure 2d).

Grain reconstruction was performed using the method as reported in our previous work (Fang *et al*., 2022b). The grain reconstruction algorithm mainly comprises two steps: 1) indexing a seeding voxel i by maximizing its completeness ($C_{seed\ i}$), defined as the number of intersected spots between forward calculation and experiment divided by the number of forward calculated spots, to derive its orientation; 2) growing a region by assigning the indexed seeding orientation to neighboring voxels that fulfil growth criteria. For a voxel j around the seeding voxel i, it will only be accepted into the grown region when its completeness ($C_{\text{voxel}\ j}$) stays above a certain percentage of $C_{seed\ i}$ and its new median distance (D_{median}) is not larger than its old value. In this work, the reconstruction parameters were kept the same for all grain reconstructions and are given in Table 2. To reconstruct grain maps for the Al matrix, a lattice parameter of 4.0498 Å with a face-centered-cubic structure and the first four {*hkl*} families, *i.e.* {111}, {002}, {022} and {113}, were used. Seeding voxels were generated iteratively with an increasing *sample gridding level*, starting from level 1 (coarse sampling with a minimum distance of 45 pixels between seeding voxels) to 11 (fine sampling with a minimum distance of 3 pixels between seeding voxels). This results in a total of ~11000 seeding voxels for testing. All the grain reconstructions were performed with a NVIDIA Tesla V100-PCIE-32GB GPU running in MATLAB software on the ESRF computing cluster. The reconstruction time varied between 12 and 48 h.

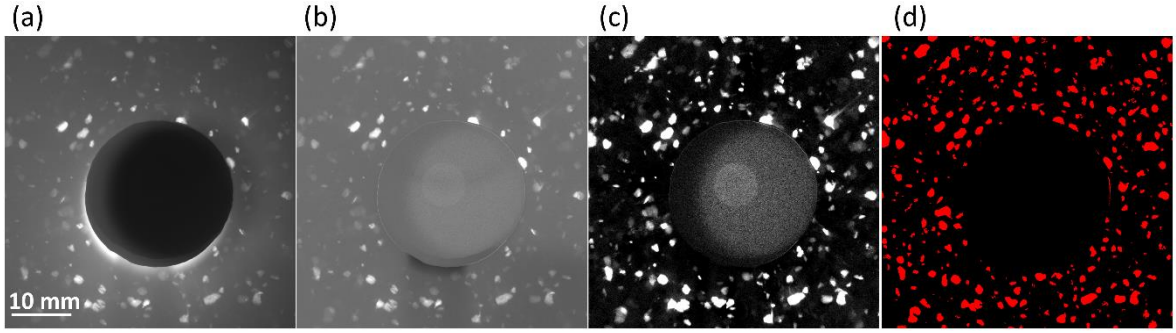

Figure 2. Processing of LabDCT images obtained from CCD measurements. (a) Experimental image averaged by 6 frames; (b) flat field corrected image; (c) image after rolling median subtraction and (d) spot segmented image where the spots are shown as red with a pixel value of 1 and the rest is shown as black with a pixel value of 0.

Notably, among the reconstruction parameters the minimum completeness (C_{min}) is most critical on the number of correctly reconstructed grains. Grain reconstructions with C_{min} values of 0.4, 0.35, 0.30 and 0.25 were performed to test the choice for this sample. The results show that the grain reconstruction with C_{min} = 0.30 gives the highest number of true positives, while no false positives

present. However, the false positives start to appear in the grain reconstruction with C_{min} = 0.25. Therefore, C_{min} = 0.30 was set for all the reconstructions in this work.

Table 2. Settings for grain reconstruction parameters that control the indexing and growth, respectively.

Type	Parameter and symbol	Value	Explanation
Indexing	Minimum completeness, C_{min}	0.30	Indexing is rejected if $C <$ pre-set value
	Maximum acceptable median distance, $maxD_{median}$	19 pixels	Indexing is rejected if $maxD_{median} >$ pre-set value
Growth	Distance tolerance of completeness weighted centers, $maxD_{center}$	3 pixels	Stop updating the center of the grown region if distance $\leq maxD_{center}$
	$\delta_{drop\text{-}off}$	0.02	Accepted into a grown region when $C_{voxel\ j} \geq (1 - \delta_{drop-off})C_{seed\ i}$

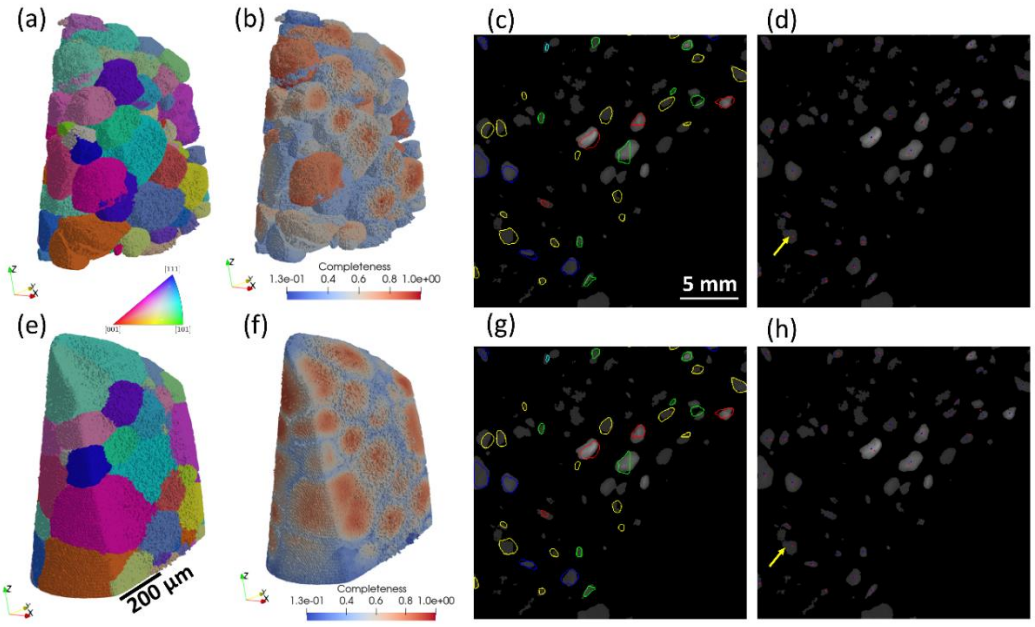

Figure 3. Grain reconstructions before (upper row) and after (bottom row) geometry fitting. (a, e) 3D grain maps colored by IPF-Z; (b, f) 3D completeness map; (c, g) outlines of forward spots overlaid onto the spot segmented images; (d, h) centers (intensity weighted) of forward (marked by red dot) and experimental (marked by blue dot) spots overlaid onto the spot segmented image.

Figure 3 shows grain reconstruction results from the CCD measurement. Notably, the grains are colored in z direction of inverse pole figure (IPF-Z) throughout the whole paper. Figure 3a shows a first grain map, reconstructed using the raw geometry and the corresponding completeness map is shown in Figure 3b. Since the goal of this initial grain map was only to fit the geometry, the reconstruction was interrupted when ~80% of the sample volume was reconstructed. To fit the geometry, relatively large

grains with relatively high completeness were selected (22 grains in this case) to perform forward simulations, from which the forward spots are overlaid onto the spot segmented image (Figure 3c). Distances between the forward and experimental spots were calculated (Figure 3d) and the fitting was subsequently carried out to minimize the average spot distance, $< D_{spot} >$, resulting in improvements in both, the overlay of the forward spots onto the experimental ones (Figure 3g) and the spot center distances (Figure 3h). Notably, experimental spots may be overlapped as marked by the yellow arrows in Figure 3d and h. This will lead to inaccurate determination of these spot centers, and thus may influence the fitting results and give an overestimation of $< D_{spot} >$. Although we tried excluding the overlapped spots from the fitting by setting up thresholds of spot distances and size differences, we cannot completely rule out those overlapped ones. Therefore, bear in mind that the derived $< D_{spot} >$ should be considered as overestimated. Table 3 summarizes the geometry parameters before and after the fittings for both, CCD and flat panel measurements.

Figure 3e shows the final grain reconstruction obtained with the fitted geometry. Figure 3f shows the corresponding completeness map. Compared to Figure 3b, an overall increase of the completeness can be seen in Figure 3f and the completeness gradient from grain central regions towards the grain surfaces is more visible. It should be noted in Figure 3f that the grains located in the bottom edge region have relatively small completeness values although they are big. This is because they suffered a partially illuminated situation, *i.e.* not always stayed in the field of view at all rotation angles during the measurement because of the circular pinhole shape.

Table 3. Geometry parameters before and after the fittings. $< D_{spot} >$ is computed from ~2000 spot pairs and the unit is in detector pixel, *i.e.* 24 µm/pixel for CCD and 127 µm/pixel for flat panel.

Type	Fitting	L_{ss} (mm)	L_{sd} (mm)	*dety*0 (mm)	*detz*0 (mm)	φ_x (°)	φ_y (°)	φ_z (°)	$< D_{spot} >$ (pixel)
CCD	Before	9.16	55.35	-0.35	1.65	0.64	0.36	0.53	6.8
	After	9.21	55.33	-0.40	1.52	-0.02	-0.21	-0.35	5.8
Flat panel	Before	9.16	224.59	0.95	-0.65	0.20	0.23	0.24	6.4
	After	9.04	224.73	0.77	-0.94	0.18	-0.15	0.57	5.7

4. Results

4.1. Comparison of grain maps between LabDCT and synchrotron DCT

Grain maps reconstructed from the flat panel and CCD measurements with the longest exposure time, *i.e.* 360 s, referred to as Lab-flat-panel and Lab-CCD, respectively, are compared with the registered grain map of synchrotron DCT measurement (SR-DCT, considered as ground truth).

Table 4 gives a summary for the indexing comparison. In both Lab-flat-panel and Lab-CCD, no false positives are found, indicating a very high indexing precision. Lab-CCD has the same number of one-to-one indexed grains as Lab-flat-panel. However, Lab-CCD has a few more one-to-multi indexed

grains, for which a relatively large grain in SR-DCT typically pairs with a large grain together with a tiny grain apart in the LabDCT grain map in this case. The average disorientations for the true positives are $\Delta_{OR} = 0.08 \pm 0.08°$ for both LabDCT datasets, with a majority of them being smaller than 0.05°. The grain centroid deviations are $\Delta_{grain} = 2.1 \pm 1.2$ pixels for Lab-flat-panel and $\Delta_{grain} = 2.4 \pm 1.1$ pixels for Lab-CCD (here 1 pixel = 2.7 μm for the sample). The obtained F_1 score values are very close between the two LabDCT datasets (see Table 4). Notably, if we exclude the false negatives on the sample surface, the F_1 score will be 1 for both datasets.

Figure 4 shows a visualization of the true positives and false negatives for the comparison between the two LabDCT datasets and SR-DCT. Compared to the true positives in SR-DCT (Figure 4a and d), most of the grains have been correctly indexed in both Lab-flat-panel (Figure 4b) and Lab-CCD (Figure 4e) and their shapes are close to SR-DCT, though with some visible differences, which are not exclusively linked to the location of false negatives. All the false negatives lie on the sample surface and they are relatively small and mostly are the same for reconstructions obtained from CCD and flat panel (Figures 4c and f).

A closer comparison is shown in Figure 5 on a selected 2D slice. Here, tomographic slices (left column in Figure 5) are also shown with an intention to demonstrate that i) grain contours obtained from SR-DCT are consistent with locations of the grain boundary precipitates (visible as bright contrast in Figure 5a) and ii) the volume registration is accurate. Comparing the 2D grain slices (middle column), Lab-CCD is more similar to SR-DCT than Lab-flat-panel, because of better grain shapes and more grains appearing in this slice. Differences in small grain regions are visible in both LabDCT grain maps and examples are marked by the yellow arrows in the completeness maps (right column), showing relatively low completeness values. We tried to use the correct grain orientations from SR-DCT to compute the completeness for these regions. The resulting completeness is found to be even smaller than the current values. This suggests that imperfect grain shapes are caused by insufficient diffraction signals rather than the reconstruction method.

Table 4. Comparison of number of indexed grains (N) between the SR-DCT dataset and the two LabDCT datasets (Lab-flat-panel and Lab-CCD). Grain size, $< D >$, is expressed as mean value and standard deviation. For one-to-multi indexed grains, the number of grains in SR-DCT is given with the paired number of grains in the LabDCT datasets given in brackets. Combined one-to-one and one-to-multi grains are considered as true positives (TP).

		N						F_1 score
Dataset	$< D >$, μm	Total indexed	One-to-one indexed	One-to-multi indexed	False-negatives (FNs)		False-positives (FPs)	
					At sample surface	In sample interior		
SR-DCT	101.4 ± 61.7	126	-	-	-	-	-	-

Lab-flat-panel	127.4 ± 73.4	79	75	2 (4)	49	0	0	0.759
Lab-CCD	122.8 ± 76.6	89	75	7 (14)	44	0	0	0.788

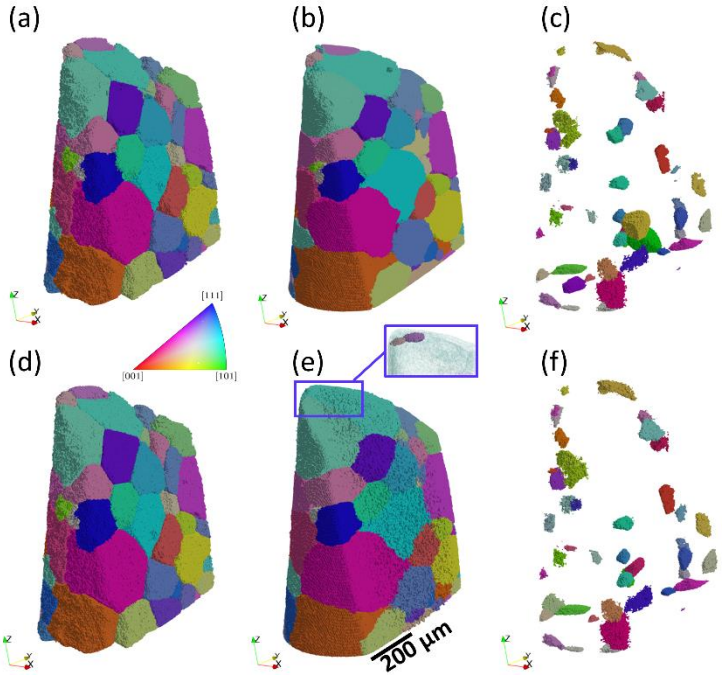

Figure 4. Comparison of grain maps between synchrotron and the two lab-based DCT datasets obtained from measurements with flat panel (upper row) and CCD (bottom row), respectively. (a, d) SR-DCT grains that are correctly indexed in the corresponding LabDCT dataset; (b, e) correctly indexed grains in the LabDCT dataset (true positives); (c, f) SR-DCT grains that are not indexed in the corresponding LabDCT dataset (false negatives). An inset in (e) makes the big green grain semi-transparent to visualize the locations of the two grains colored in light and dark pink at the top.

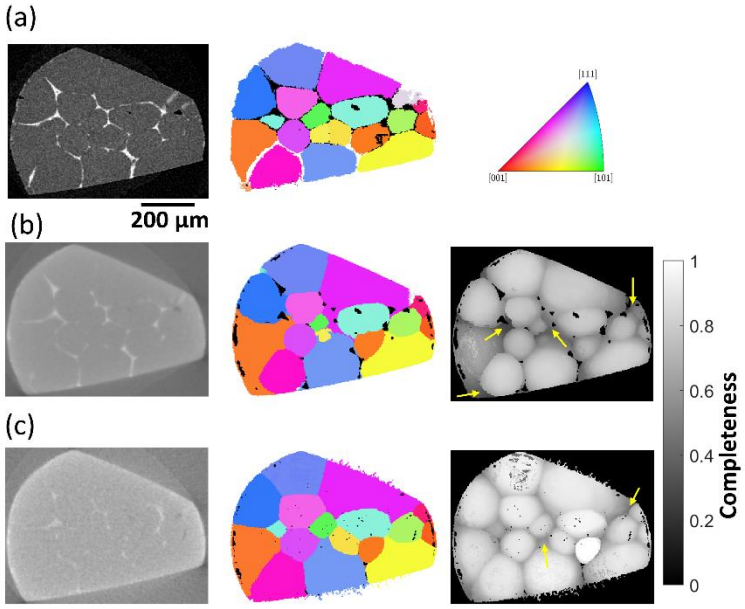

Figure 5. Comparison of 2D sections from tomography volumes and grain maps shown on the left and middle columns, respectively, and the corresponding completeness map shown on the right column. (a) Synchrotron dataset, (b) Lab-flat-panel and (c) Lab-CCD.

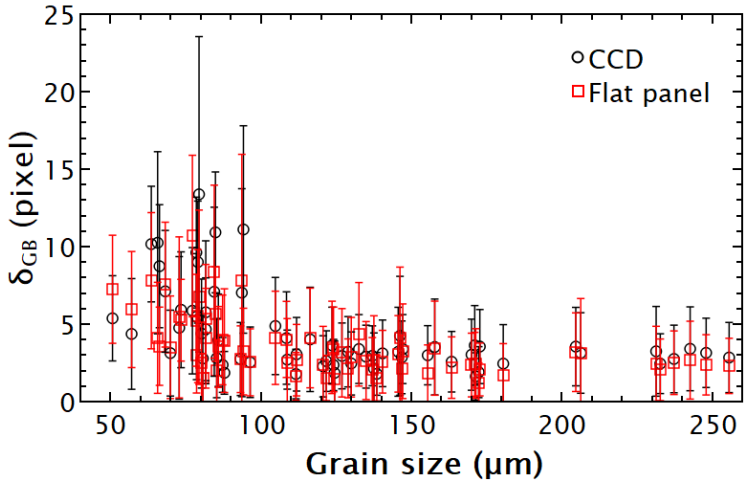

Figure 6. Grain boundary deviation (δ_{GB}) as a function of grain size for Lab-CCD and Lab-flat-panel. Error bars correspond to the standard deviations of δ_{GB}. Here 1 pixel corresponds to 2.7 µm.

Figure 6 shows grain boundary deviation (δ_{GB}) as a function of grain size for 69 commonly indexed grains to quantify the accuracy of the reconstructed grain shapes with respect to SR-DCT. The figure shows that δ_{GB} behaves similarly in the two LabDCT datasets, remaining as a constant of 2 ~ 3 pixels (δ_{GB} = 2.97 ± 2.30 pixels for Lab-CCD and δ_{GB} = 2.64 ± 2.38 pixels for Lab-flat-panel with 1 pixel = 2.7 µm) when grain size > 100 µm, below which δ_{GB} starts to increase. Similar behavior has also been observed in the work of (Fang, Juul Jensen *et al*., 2021; Fang, Hovad *et al*., 2021) and is considered as a general characteristic for the LabDCT technique. Reason for increasing δ_{GB} with decreasing grain size below a certain size is mainly due to poorer diffraction signals, resulting in worse spot segmentation and fewer spots to be successfully segmented. These further lead to bigger errors in the determination of the spot centers and shapes, thereby influencing the grain boundary accuracy.

Another consequence of the poorer signals is that large neighboring grains may have higher completeness and "grow" into the regions which should have been occupied by the small missing grains. This has been observed as marked by yellow arrows in Figure 5.

4.2. Contrast-to-noise ratio as a function of exposure time

Contrast-to-noise ratio (*CNR*) is determined for individual spots in raw frames before any image processing and the calculation method is illustrated in *Appendix*. Figure 7 shows *CNR* as a function of exposure time (t_{exp}) for four {111} spots from grains with different size levels. It can be seen in Figure 7a that *CNR* saturates in ~20 s for all the four spots from the flat panel measurements, whereas *CNR* saturates at different times for the CCD data as shown in Figure 7c. Comparing the *CNR* values in Figure 7a and c, the values from the CCD measurement are significantly higher than those from the flat

panel measurement. Although the *CNR* values are rather low as plotted in Figure 7a, the spots can still be identified and segmented except for the spot 4 (from a small grain) as shown in Figure 7b. Given higher *CNR* values, the spot segmentation looks more accurate for the CCD measurement (Figure 7d).

Interestingly, whether or not a spot can be successfully segmented is not linearly proportional to its *CNR* value. As shown by spot 4 in the flat panel measurement, it is not segmented but it has a higher *CNR* value (~ 0.8 at t_{exp} = 360 s) than spots 2 and 3 (~ 0.5 at t_{exp} = 360 s), both of which are segmented. The reason is that the final spot segmentation not only depends on the *CNR* in the raw image, but also depends on the subsequent processing (flat field correction, rolling median and filtering *etc*.). This means the spot segmentation may also be influenced by local spot regions as well as global background intensity. By tracking additional spots, it is found that spots with *CNR* < 1 have high chance to be not segmented and *CNR* values vary dramatically even for the same grain, depending on spot energy, *hkl* reflection, rotation angle ω and the spot location on the detector (corners have higher background noise than inner region).

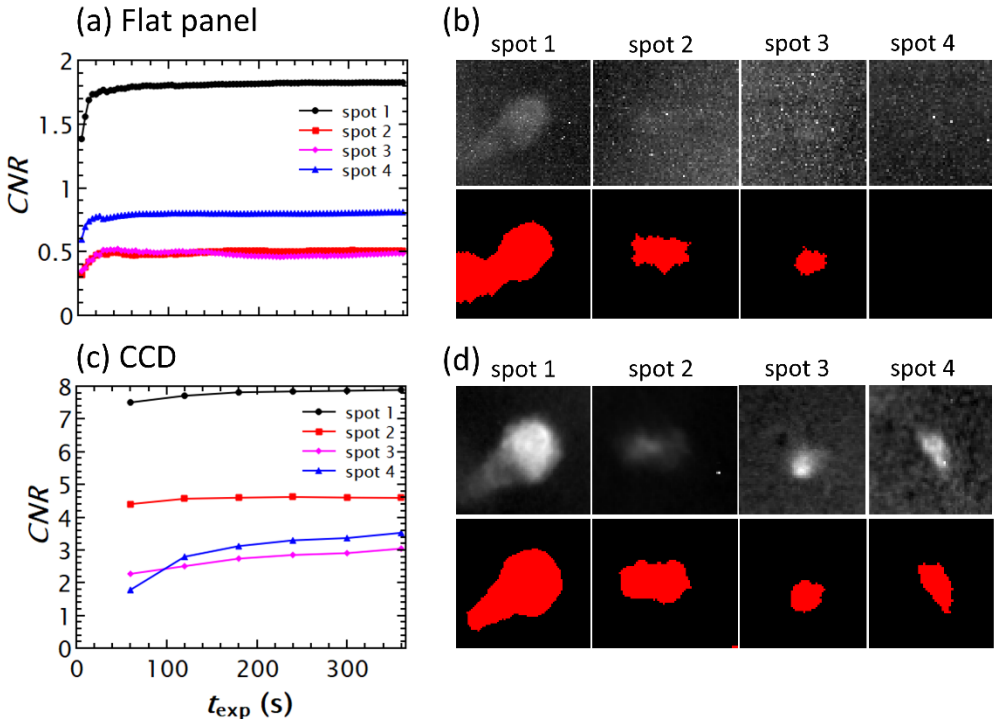

Figure 7. Contrast-to-noise ratio (*CNR*) as a function of exposure time for four spots tracked in both (a) flat panel and (c) CCD measurements. The spot cropped images obtained from t_{exp} = 360 s (upper row) and the corresponding spot segmented images (lower row) are shown in (b) for flat panel and (d) for CCD measurements. Spot 1 corresponds to grain #25, 1 -1 -1, rotation angle ω = 288°, average spot energy E_{spot} = 18.2 keV; Spot 2: grain #79, -1 1 -1, ω = 288°, E_{spot} = 14.3 keV; Spot 3: grain #111, 1 -1 1, ω = 273°, E_{spot} = 16.3 keV; Spot 4: grain #142, 1 1 1, ω = 216°, E_{spot} = 18.9 keV. The sizes of grain #25, #79, #111 and #142 are 163.4, 85.3, 57.0 and 36.4 µm, respectively. Grain #25, #79 and #111 are all indexed in the LabDCT datasets, whereas grain #142 is not, in neither one.

Figure 8 shows raw LabDCT images from the flat panel measurement and the corresponding spot segmented images for t_{exp} = 4, 20, 60, 120 and 360 s. It can be clearly seen that the number of segmented spots increases with increasing t_{exp} (the number of spots is 190, 240, 268, 292 and 343 in Figure 8a – e, respectively). Zoom-ins of one large spot (that is spot 1 in Figure 7) show that its background noise is significantly reduced from t_{exp} = 4 to 20 s, then it does not change too much, as can also be seen from the segmented shapes.

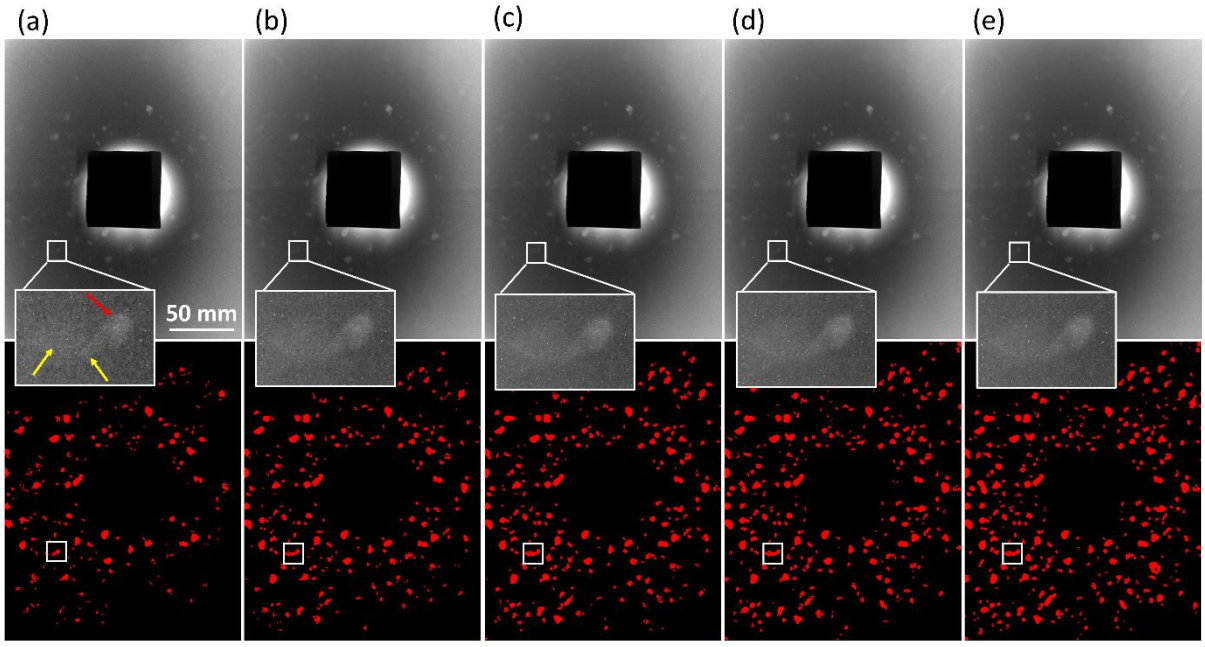

Figure 8. Raw LabDCT images acquired by flat panel (upper row) and the corresponding spot segmented images (bottom row) at ω = 288°. Images are averaged by 1, 5, 15, 30 and 90 frames in (a – e), corresponding to an exposure time of 4, 20, 60, 120 and 360 s, respectively. Zoom-ins show the spot 1 -1 -1 from grain #25 (marked by the red arrow in (a); see its *CNR* in Figure 7) and white boxes mark the corresponding segmentation in the bottom images. Note that the spot of interested is partially overlapped with two other spots (marked by the yellow arrows in (a)), hence they are segmented as one single spot.

4.3. Grain reconstruction as a function of exposure time

Grain maps are reconstructed from LabDCT images with different exposure time for both flat panel and CCD. Figure 9 shows a comparative view of the grain maps. It can be seen in Figure 9a that grain volume increases with increasing t_{exp}, with more and more relatively small grains being reconstructed. Grain shapes are also improving to be more and more conforming to the empty space with increasing t_{exp}. Notably, the majority of the grains are reconstructed even with t_{exp} = 4 s for the flat panel. When t_{exp} increases to 20 s, the sample volume is nearly filled and this filling ratio continues to improve with longer exposure time. For the CCD measurement, the shortest resolved exposure time in

this work is 60 s. It can be seen in Figure 9b that the grain map quality with t_{exp} = 60 s is already quite close to the best one (t_{exp} = 360 s). Comparing Figure 9a and b, a similar relationship of grain map quality is observed as a function of t_{exp} when its value ≥ 60 s between the flat panel and CCD reconstructions.

Quantitative indexing comparison is summarized in Table 5. The table shows that more and more grains are correctly indexed with increasing t_{exp} for both detectors. 88% of the grain volume is reconstructed with t_{exp} = 4 s for the flat panel and 98% is reconstructed when t_{exp} = 20 s for the flat panel and 60 s for the CCD.

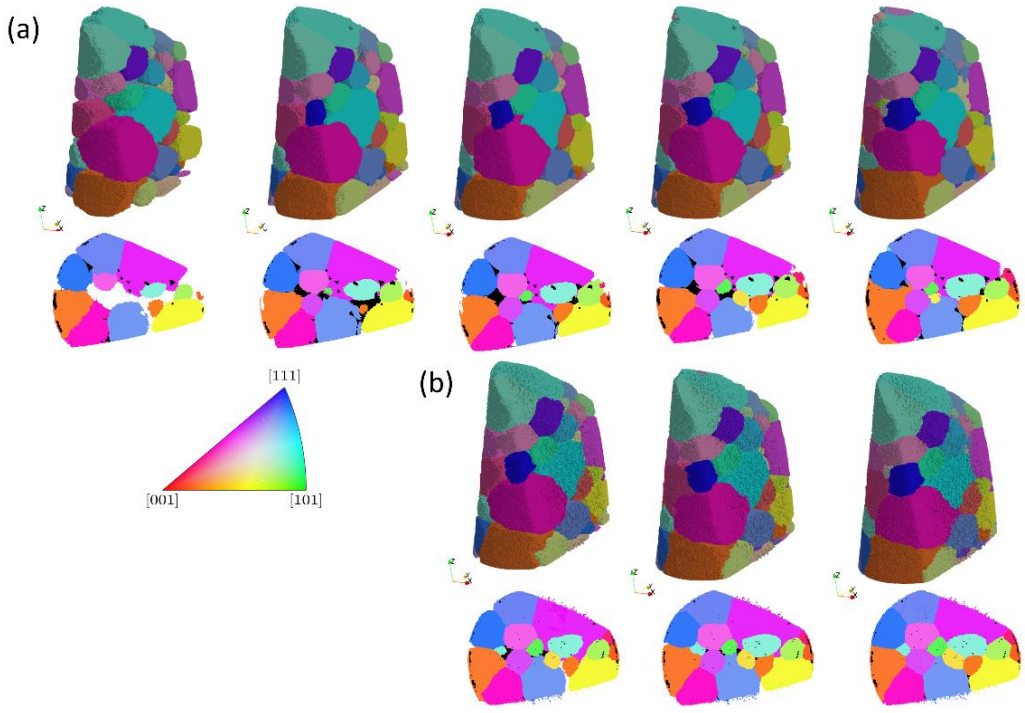

Figure 9. Comparison of grain reconstructions with different exposure time for measurements of (a) flat panel (left to right: t_{exp} = 4, 20, 60, 120 and 360 s, respectively) and (b) CCD (left to right: t_{exp} = 60, 120 and 360 s, respectively).

Table 5. Indexing comparison for grain reconstructions with different exposure time with respect to SR-DCT. $f_{indexed}$ / $f_{indexed}$ (360 s) denotes the ratio of the reconstructed volume with respect to the volume with the longest exposure time of 360 s. Other symbols have the same meanings as in Table 4.

Dataset			*N*				F_1 score	$f_{indexed}$ / $f_{indexed}$ (360 s)
	t_{exp} (s)	< *D* >, μm	Total indexed	One-to-one indexed	One-to-multi indexed	*FN*s		
Flat panel	4	146.8 ± 79.9	50	45	3 (6)	78	0.552	0.8854
	20	146.7 ± 73.9	59	56	2 (4)	68	0.630	0.9768
	60	140.7 ± 73.9	65	63	1 (2)	62	0.674	0.9875
	120	141.7 ± 71.1	66	66	0	60	0.688	0.9864
CCD	60	144.5 ± 71.6	68	62	3 (6)	61	0.681	0.9774
	120	141.2 ± 73.8	71	69	1 (2)	56	0.714	0.9835

5. Discussions

5.1. Detection limit and spatial resolution of the current LabDCT

It can be seen from Figures 4 and 5 and Table 4 that the current LabDCT implementation on the AlCu sample is capable of resolving all the relatively large grains, but has a detection limit of ~ 50 µm, below which the reconstruction fails. To explain this, the completeness is plotted as a function of grain size using grain maps from both LabDCT and SR-DCT as inputs. Figure 10a shows the completeness values for all the reconstructed grains from Lab-CCD, together with the values for grain centroids of the true positives and false negatives in SR-DCT. The figure shows that most of the false negatives have completeness values smaller than 0.3, which is the minimum completeness for the reconstruction. Three false negatives have a completeness value slightly above 0.3, which would be expected to be reconstructed ideally. However, the reason for not being able to reconstruct these grains is that the completeness values are indeed higher with other grain orientations than using orientations of these grains. This indicates that the grain reconstruction algorithm does not hinder the improvement of the detection limit; it is detectability of the diffraction signals controlling the current detection limit. A similar behavior is seen in Figure 10b for the flat panel, where the completeness values for most of the false negatives fall below 0.3 and the other five have values above. The latter has the same reason as the CCD data. Notably, in both Figure 10a and b, one true positive with a grain size of 50.7 µm has a much higher completeness from both LabDCT datasets than SR-DCT. This is found to be due to a significantly different orientation (a disorientation of ~ 0.4°). Upon closer inspection of the SR-DCT dataset, the corresponding grain shows a distinct sub-grain structure and one of these subgrains has been indexed in SR-DCT as an additional small grain with a misorientation of 0.45°.

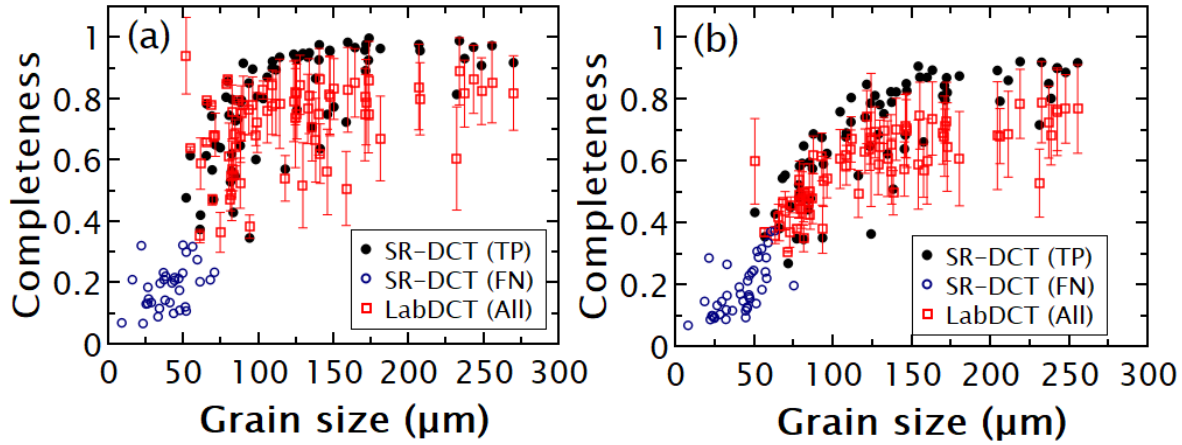

Figure 10. Completeness as a function of grain size for measurements of (a) CCD and (b) flat panel. Completeness values are plotted as an average and an error bar for all the LabDCT grains, while only the grain centroid completeness is plotted for SR-DCT grains. These grains are classified into true positives (*TP*) and false negatives (*FN*).

The spatial resolution, expressed by the grain boundary deviation (similar to Fang, Juul Jensen *et al*., 2021; Fang, Hovad *et al*., 2021), is at a constant level of 2 ~ 3 pixels (5 ~ 8 μm), showing a reasonably good performance. However, the spatial resolution becomes worse when grain size gets smaller than 100 μm (see Figure 6). This is related to the number of spots for reconstruction. As can be seen in Figure 10, the completeness values also start to decrease from a relatively constant value with decreasing grain size below than 100 μm, corresponding to fewer spots detected/segmented for reconstruction.

5.2. Characteristics of variable detectors

The grain maps reconstructed from the flat panel and the CCD measurement data are somewhat comparable, although the CCD gives a marginal improvement in the grain indexing (see the F_1 score in Table 4). However, given the contrast-to-noise ratio for the CCD is much higher than the flat panel (see Figure 7), one would expect that the performance of both, the detection limit and spatial resolution for the CCD must be significantly better than the flat panel. There are mainly two reasons: 1) spot segmentation is not linearly proportional to CNR as explained in Section 4.2; 2) the flat panel covers a bigger range of scattering angles and thus records more spots than the CCD. Assuming a diffraction event occurs at the origin, the flat panel measurement covers a scattering angle (2θ) range from 7.4 to 33.6°, while 2θ is in the range of 12.5 – 32.0° for the CCD measurement. Although the maximum accessible angle ($2\theta_{max}$) is only slightly bigger, the flat panel has a significantly smaller $2\theta_{min}$, which is beneficial for recording spots from lower order $\{hkl\}$ reflections (usually brighter spots). This suggests that a detector with a larger recording area can be preferable in presence of geometrical constraint (minimum distances of L_{ss} and L_{sd}) limiting the accessible 2θ range.

As shown in Figure 11a, the completeness values for all the four selected grains, regardless of being indexed or not in the LabDCT datasets, are always lower in the flat panel measurements than the CCD measurements for the same exposure time. This is consistent with the plots of contrast-to-noise ratio (see Figure 7). However, Figure 11b shows that the number of intersected spots are actually higher in flat panel data than the CCD. This means that more spots were used for reconstructing the grain shapes and partly explains why the spatial resolution of the flat panel measurement is very close to the CCD measurement. Figure 11 also explains the observation in Figure 9 that the grain maps are continuously improving with increasing exposure time, although it looks the *CNR* quickly saturates for some individual spots, *e.g.* within 20 s for the flat panel.

It is found that the two detectors have different advantages and disadvantages. Compared to the CCD, the flat panel has lower sensitivity to the diffraction signals and has a larger pixel size, thus requires a longer L_{sd} to achieve comparable effective pixel size. However, the flat panel is much cheaper and easier to be implemented (*e.g*. no cooling is required) and has a faster readout time. Since our grain reconstruction method is working on spot binarized images rather than on spot intensities, the poorer sensitivity of the flat panel does not cause too much harm in the final grain map quality, as demonstrated

in the present AlCu alloy sample that the quality is comparable to the CCD result. Nevertheless, the CCD has a better sensitivity and gives better contrast-to-noise ratios, making it more advantageous in increasing the completeness value for a given grain size.

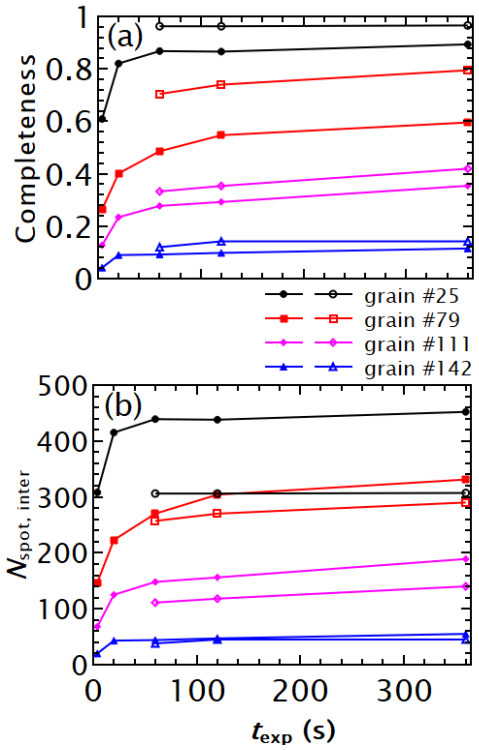

Figure 11. (a) Completeness and (b) number of intersected spots ($N_{spot,\ inter}$) between forward simulation and experiment as a function of exposure time for four selected grains, whose *CNRs* are plotted in Figure 7. Closed symbols correspond to the flat panel data, while the open symbols correspond to the CCD.

5.3. Geometry optimization

Whilst geometry optimization for the LabDCT experiments presented in this work has been mostly emphasized on the sample-to-detector distance (see Supplementary Materials), considerations on the sample-to-source distance, the position/choice of the aperture to confine the incident beam and the beamstop to cover the footprint of the direct beam are also important to optimize the LabDCT geometry. For the basic acquisition protocol described here (*i.e.* single rotational scan of a fully illuminated sample cross-section), the dimensions of the sample may have to be adapted to the grain size of the material so as to limit the through-thickness dimension to about 10 grain diameters in order to limit diffraction spot overlaps on the detector. Shorter source-to-sample distances will increase the photon flux at the sample position, but also lead to a wider opening angle of the cone beam and hence reduced area for the collection of diffraction signals on the detector – a compromise has to be found here. The sample and the aperture should be placed close to the source for increasing the photon flux at the sample position. Placing the aperture close to the sample allows to reduce scattering and fluorescence

from the aperture itself, thereby reducing the high background area close to the direct beam and increasing the effective area for detecting diffraction spots on the detector. Notably, the use of a circular aperture as in the current implementation is not optimal, because it can lead to partial illumination of sample sub-volumes as described in Section 3. A selection of rectangular windows with variable aspect ratios would provide better flexibility to adapt to samples of different dimensions and grain size.

The choices of the sample-to-detector distance and the beamstop should take into account of a combination of the diffraction angle coverage, effective pixel size in the sample plane, footprint size of the direct beam, spot contrast-to-noise ratio and probability of spot overlap. These parameters altogether may not be straightforward to be sort out for an optimal geometry setting, whilst they strongly depend on sample characteristics and scientific questions associated with the sample. In practice, tests of diffraction projections with different combinations of choices may be useful to select a geometry setting to perform decent LabDCT experiments for a given sample.

5.4. Outlook for future development of the LabDCT technique

It is demonstrated that "fast" grain mapping by LabDCT is possible. As shown in Figure 9 and Table 5, 88% of the grain volume is reconstructed with an exposure time of 4 s. This corresponds to a dramatic decrease in total scanning time from typically ~12 h to only ~10 min for 121 LabDCT projections. Even with the exposure time increasing to 20 s, the total scanning time will be less than 1 h, while the grain map quality will be significantly improved, *e.g.* 98% of the grain volume was reconstructed. This much shorter scanning time will make LabDCT measurement compatible with the scanning time of conventional tomography scans using lab-based X-rays. Therefore, it opens the possibility to perform *time-lapse* LabDCT observations of processes like grain growths on conventional X-ray instruments.

Whilst the spatial resolution is rather close, the detection limit of the current LabDCT implementation on the conventional tomography setup is inferior to the commercial one, *e.g.* Zeiss Xradia 520 Versa (Fang, Juul Jensen *et al*., 2021; McDonald *et al*., 2021). This is mainly due to the usage of different sources and detector systems. A measurement on the spectrum of the X-ray source for the current instrument shows that the spectrum has a peak intensity around 10 keV (related to L_α edge of tungsten anode material) and is not yet optimal for maximizing the performance of the LabDCT technique. Although different materials favor high fluxes at different energy ranges, it is preferable to have continuous high fluxes in the energy range of 15 - 80 keV for measuring typical metallic materials.

Improving detective quantum efficiency and reducing background noise is also an effective approach to improving the detection limit for LabDCT. New direct photon counting detectors show promising results in X-ray imaging and tomography (*e.g*. Bellazzini *et al*., 2015; Ballabriga *et al.*, 2020). With these detectors, ideally, it is expected to have sharp images with very low background noise and very small point spread, and even have a capability to resolve X-ray energies with the so-called 'color' detectors. In practice, we also tested a prototype CdTe direct photon counting detector for LabDCT grain

mapping. The recorded diffraction images were indeed sharp and with a smaller point spread compared to both the flat panel and CCD. However, the dimension of this CdTe detector, as well as some other issues related to the use of this detector make the final performance not optimal yet. Nevertheless, it can be anticipated that this new generation of detectors will lead to significant improvements of the LabDCT technique.

There is room to further develop the reconstruction algorithm for improving the detection limit. Currently, a single value for the minimum completeness is used to determine the acceptance or rejection of an orientation indexing. In general, this value should not be too high to miss true positives, and also should not be too low to induce the reconstruction of false positives. As shown in Figure 10, small grains inevitably have low completeness values, making them more susceptible to be not indexed successfully. This means that the smallest reconstructed grain in the final grain map would be generally bigger than the size inferred from the smallest spot detected on the detector, because its maximum completeness value is more likely to be smaller than the minimum completeness value threshold. One possible way to overcome this limit is to perform successive reconstructions with decreasing minimum completeness parameter values. At each iteration the spots that can be reliably paired with the already-indexed grains will be removed. By this way, rather low minimum completeness values can be used to favor the reconstruction of the small grains and simultaneously reduce the probability of reconstructing false positives. Ultimately, a smaller detection limit could be achieved.

The current reconstruction algorithm works on spot binarized images, *i.e.* independent of spot intensities. This is very efficient for reconstructing grain maps, and beneficial for measurement data when the contrast-to-noise ratios of the diffraction spots are low but still segmentable (*e.g.* the flat panel data in this work). However, working on binarized images also means that intra-granular orientations within individual grains cannot be retrieved. To expand the current LabDCT technique from only strain-free samples to deformed samples, a further development of the reconstruction algorithm taking into account the spot intensities will be required.

6. Conclusions

In this study, a successful implementation of grain mapping by LabDCT has been demonstrated on a conventional tomography setup using a flat panel detector and a CCD. The grain reconstruction procedure using our previously developed method is presented in detail. The obtained grain maps from an AlCu alloy sample were compared with the ground truth from the synchrotron measurement. Contrast-to-noise ratios are studied as a function of exposure time and the resulting grain reconstructions are quantitatively assessed. A comprehensive discussion on the current performance, characteristics of different detectors and the outlook is presented. The main conclusions are listed as follows.

1) The grain maps from the LabDCT measurements are reasonably well reconstructed with respect to the synchrotron ground truth. Most of the grains are correctly reconstructed with an average orientation accuracy of ~0.08° and a spatial resolution of 2 ~ 3 pixels (*i.e.* 5 ~ 8 μm) for grains larger

than 100 μm, whilst grains smaller than 50 μm in this sample are beyond the detection limit of the current implementation.

2) Although the CCD detector has significantly better contrast over noise ratio as compared to the flat panel, the quality of the resultant grain maps is almost identical except for a marginal improvement in grain indexing for the CCD detector for the sample studied in present work. This demonstrates a high tolerance of the detector choice for implementing LabDCT on conventional tomography setups.

3) The reasons for having comparable grain reconstruction quality between the flat panel and the CCD measurements are twofold: First, the quality of spot segmentation is not linearly proportional to the contrast-to-noise ratio. Second, although the completeness values are lower, the absolute number of spots per grain is higher in the flat panel measurement because it covers a wider range of scattering angles.

4) Given the superior contrast to noise ratio of the CCD detector, it can be anticipated that further optimization of the acquisition geometry, including source to sample distance, pinhole position and dimensions would have allowed to overcome the grain size detection limit reported in the current study.

5) 88% of grain volume is reconstructed with a very short exposure time of 4 s using the flat panel, opening the possibility of *in-situ* LabDCT experiments. With further increasing the exposure time to 20 s, 98% of the grain volume is reconstructed and the total data acquisition time can be confined to less than one hour.

Given the experimental demonstration with different detectors presented here and an open-sourced reconstruction code (https://gricad-gitlab.univ-grenoble-alpes.fr/TomoX_SIMaP/GrainRecon), 3D grain mapping by LabDCT or other variants using white/pink X-ray or neutron beam will be easier to be established on other instruments and more widely accessible.

Appendix. Determination of contrast-to-noise ratio for diffraction spot

Contrast-to-noise ratio is determined by performing a forward projection onto the experimental raw images, as illustrated in Figure 12. First, the forward spot is overlaid onto the experimental image and a region of interest is defined as the bounding box of the forward spot oversized by 20 pixels. Then, the masked region by the forward spot is regarded as “spot”, whose average pixel value is calculated ($\bar{I}_{spot}$). The rest region is regarded as “background”, whose average and standard deviation of the pixel values are calculated ($\bar{I}_{bg}$ and σ_{bg}, respectively). Last, *CNR* is calculated as

$$CNR = \frac{\bar{I}_{spot} - \bar{I}_{bg}}{\sigma_{bg}}. \quad (2)$$

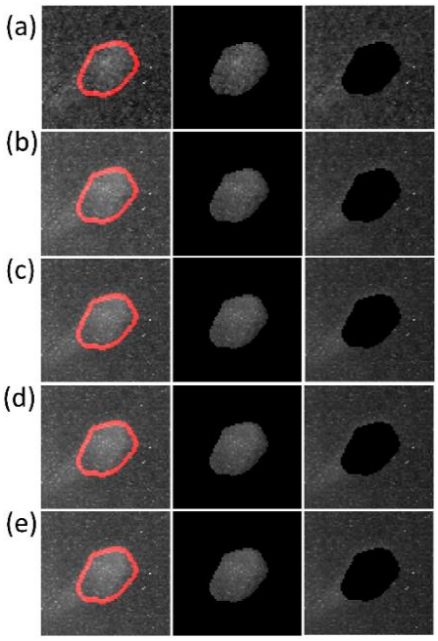

Figure 12. Illustration of determining contrast-to-noise ratio (*CNR*) for the spot 1 -1 -1 at $\omega = 288°$ from grain #25 (see its *CNR* values for spot 1 in Figure 7a) in images measured by flat panel with an exposure time of (a) 4 s, (b) 20 s, (c) 60 s, (d) 120 s and (e) 360 s, respectively. Left column: a forward spot overlaid onto the experimental image; middle column: region masked by the forward spot to identify the experimental spot; right column: the rest region to determine background noise. Note that another smaller diffraction spot is present at the left-lower corner of the spot of interest, being partially overlapped with each other.

Acknowledgement

The authors are grateful to Dr. Rémi Granger for making the pinhole mounting system available on the tomography instrument and Prof. Luc Salvo for providing the raw material to prepare the AlCu alloy sample used in the present work. W.L. acknowledges ESRF for granting inhouse beam time for measurement of the SR-DCT dataset and provision of computing resources.

Funding information

This work receives funding from the Agence Nationale de la Recherche through the project Advanced Laboratory X-ray Microtomography (ANR-18-CE42-0005). SIMAP is part of LabEx CEMAM (ANR-10-LABX-44-01).

References

Bachmann, F., Bale, H., Gueninchault, N., Holzner, C. & Lauridsen, E.M. (2019). *J. Appl. Cryst.* **52**, 643-651.

Bachmann, F., Hielscher, R. & Schaeben, H (2010). *Solid State Phenomena* **160**, 63-68.

Ballabriga, R., Alozy, J., Bandi, F.N., Campbell, M., Egidos, N., Fernandez-Tenllado, J.M. *et al*. (2020). *IEEE Trans. Radiat. Plasma Med. Sci*. **5**, 422-440.

Bellazzini, R., Brez, A., Spandre, G., Minuti, M., Pinchera, M., Delogu, P., de Ruvo, P.L. & Vincenzi, A. (2015). *J. Instrum*. **10**, C01032.

Bernier, J. V., Barton, N. R., Lienert, U. & Miller, M.P. (2011). *J. Strain. Anal. Eng. Des.* **46**, 527-547.

Bhattacharya, A., Shen, Y.F., Hefferan, C.M., Li, S.F., Lind, J., Suter, R.M., Krilliii, C.E. & Rohrer, G.S (2021). Science **374**, 189-193.

Fang, H., Juul Jensen, D. & Zhang, Y. (2020). *Acta Cryst. A* **76**, 652-663.

Fang, H., Juul Jensen, D. & Zhang, Y. (2021). *IUCrJ* **8**, 559-573.

Fang, H., Hovad, E., Zhang, Y., Clemmensen, L.K.H., Kjaer Ersbøll, B. & Juul Jensen, D. (2021). *IUCrJ* **8**, 719-731.

Fang, H., Granger, R., Ludwig, W. & Lhuissier, P., (2022). *IOP Conf. Ser. Mater. Sci. Eng*. 1249, 012039.

Fang, H., Ludwig, W. & Lhuissier, P. (2022). *J. Appl. Cryst*. **55**, 1652-1663.

Hayashi, Y., Setoyama, D., Hirose, Y., Yoshida, T. & Kimura, H. (2019). *Science* **366**, 1492-1496.

Henningsson, N.A., Hall, S.A., Wright, J.P. & Hektor, J. (2020). *J. Appl. Cryst*. **53**, 314-325.

Jakobsen, A.C., Simons, H., Ludwig, W., Yildirim, C., Leemreize, H., Porz, L., Detlefs, C. & Poulsen, H.F. (2019). *J. Appl. Cryst* **52**, 122-132.

King, A., Johnson, G., Engelberg, D., Ludwig, W. & Marrow, J. (2008). *Science* **321**, 382-385.

King, A., Reischig, P., Adrien, J. & Ludwig, W. (2013). *J. Appl. Cryst.* **46**, 1734-1740.

King, A., Reischig, P., Adrien, J., Peetermans, S. & Ludwig, W. (2014). *Mater. Character.* **97**, 1-10.

Larson, B.C., Yang, W., Ice, G.E., Budai, J.D. & Tischler, J.Z. (2002). *Nature* **415**, 887-890.

Lind, J. F. (2013). PhD thesis, Carnegie Mellon University, Pittsburgh, Pennsylvania, USA.

Lindkvist, A., Fang, H., Juul Jensen, D. & Zhang, Y. (2021). *J. Appl. Cryst.* **54**, 99-110.

Ludwig, W., Schmidt, S., Lauridsen, E.M. & Poulsen, H.F. (2008). *J. Appl. Cryst*. **41**, 302-309.

Ludwig, W., Reischig, P., King, A. Herbig, M., Lauridsen, E.M., Johnson, G., Marrow, T.J. & Buffière, J.Y. (2009). *Rev. Sci. Instrum*. **80**, 033905.

McDonald, S. A., Reischig, P., Holzner, C., Lauridsen, E.M., Withers, P.J., Merkle, A.P. & Feser, M. (2015). *Sci. Rep*. **5**, 14665.

McDonald, S.A., Holzner, C., Lauridsen, E.M., Reischig, P., Merkle, A. & Withers, P.J. (2017). *Sci. Rep.* **7**, 5251.

McDonald, S. A., Burnett, T. L., Donoghue, J., Gueninchault, N., Bale, H., Holzner, C., Lauridsen, E.M. & Withers, P.J. (2021). *Mater. Character.* **172**, 110814.

Oddershede, J., Bachmann, F., Sun, J. & Lauridsen, E.M. (2022). *Integr. Mater. Manu. Inno.* **11**, 1-12.

Offerman, S.E., van Dijk, N.H., Sietsma, J., Grigull, S., Lauridsen, E.M., Margulies, L., Poulsen, H., Th. Rekveldt, M. & van der Zwaag, S. (2002). *Science* **298**, 1003-1005.

Poulsen, H.F. (2004). *Three-dimensional X-ray diffraction microscopy: mapping polycrystals and their dynamics*, Springer, Berlin.

Poulsen, H.F., Jakobsen, A.C., Simons, Ahl, S.R., Cook, P.K. & Detlefs, C. (2017). *J. Appl. Cryst*. **50**, 1441-1456.

Poulsen, H.F. (2020). *Curr. Opin. Solid State Mater. Sci*., 100820.

Reischig, P., King A., Nervo L., Viganó, N., Guilhem, Y., Palenstijn, W.J., Batenburg, K.J., Preuss, M. & Ludwig, L. (2013). *J. Appl. Cryst*. **46**, 297-311.

Renversade, L., Quey, R., Ludwig, W., Menasche, D., Maddali, S., Suter, R.M. & Borbely, A. (2016). *IUCrJ* **3**, 32-42.

Schmidt, S., Nielsen, S.F., Gundlach, C., Margulies, L., Huang, X. & Juul Jensen, D. (2004). *Science* **305**, 229-232.

Simons, H., King, A., Ludwig, W., Detlefs, C., Pantleon, W., Schmidt, S., Stöhr, F., Snigireva, I., Snigirev, A. & Poulsen, H.F. (2015). *Nature Comm*. **6**, 6098.

Simons, H., Haugen, A.B., Jakobsen, A.C., Schmidt, S. et al. (2018). *Nature Mater*. **17**, 814-819.

Suter, R.M., Hennessy, D., Xiao, C. & Lienert, U (2006). *Rev. Sci. Instr*. **77**, 123905.